Investigating Structural Controls on the Heat Flux and Steam Release from the Waiotapu Geothermal Field using the Landsat 9 Dataset

Emmanuel Turinimana[1], Gerd Sielfeld[1], Thomas Dowling[1], James D. Muirhead[1], Julie V. Rowland[1], Shane Cronin[1], and Alexander Gold[1]

[1]University of Auckland, Private Bag 92019, Auckland 1142, New Zealand

etur893@aucklanduni.ac.nz

Keywords: *Structure, heat, steam, rift, Landsat.*

ABSTRACT

Geological (tectonic and volcanic) structures control the flow of hot fluids in rift settings. Geothermal fluids transported to the surface through permeable pathways bring heat energy associated with steam release that can be examined by mapping anomalously hot areas. This study explores the structural influence on the spatial pattern of the surface heat flux and the total heat and steam released from the ground at the Waiotapu geothermal field. We investigated structural fabrics and spatial patterns of surface heat flux from the Waiotapu geothermal field, the largest of 20 major high-temperature geothermal fields in the Taupō Volcanic Zone (TVZ), New Zealand. Landsat 9 datasets and ground measurements were processed and analysed using Python and QGIS to calculate land surface temperatures for the Waiotapu area and its surroundings. Land surface temperatures are used to estimate heat fluxes. The spatial distribution of heat fluxes at Waiotapu and its surroundings correlates well with mapped structural features using the 30 m-resolution Shuttle Radar Topography Mission (SRTM) DEM dataset. This indicates that tectonic and volcanic structures control the spread of heat flux anomalies. The total heat flux from the land surface and associated steam release at Waiotapu is calculated as 547.5 ± 20.1 MW. This high value underscores the role of the geothermal field contribution to the heat and steam budget of this rift and the overall importance of the Taupō Volcanic Zone influence on the atmosphere.

1. INTRODUCTION

Geological (tectonic and volcanic) structures occurring in intra-arc rift settings, particularly the Taupō Volcanic Zone (TVZ), have been shown to facilitate the transfer of heat by the movement of hot fluids (Rowland & Simmons, 2012; Wilson& Rowland, 2016). Tectonic and volcanic activity affect the hydrothermal fluid flow mainly through fault-fracture network permeability, pipelike vertical conduits produced by eruptions, and heat from magmatic intrusions (Rowland & Sibson, 2004; Rowland & Simmons, 2012). Surface heat loss from hot fluid circulation can be constrained from terrestrial-based measurements and remote sensing data to provide information and insight into the size and dynamics of the underlying geothermal resource (Hochstein & Bromley, 2005**;** Seward et al., 2025). At rifted settings, both intra-arc and continental rifts, the spatial pattern of heat flux is influenced by tectonic and volcanic structures like fault and fracture networks, caldera rim structures, and volcanic cones and lineations.

Heat transfer from the subsurface of the hot anomalous areas to the surface occurs through various mechanisms, and various approaches exist for measuring the heat flux in geothermal and volcanic areas (Wang & Pang, 2023). Heat is mainly transferred through conduction and advection in the subsurface (Seward et al., 2025). The surface heat loss takes place through conduction and convection through heated ground, discharge of heated fluids from springs, seeps, and pools, and evaporation, radiation, and conduction from the surface of geothermal water bodies (Wang & Pang, 2023**;** Seward et al., 2025). The established techniques for heat flux measurements include using: satellite infrared sensors (Darge et al., 2019), thermal infrared remote sensing of radiative heat loss (Bromley et al., 2015; Seward et al., 2018), calorimeter measurements (Hochstein & Bromley, 2005), CO_2 surface emissions (Fridricksson et al, 2006; Yang et al., 2024), interpreting ground temperature-depth profiles (Wang et al., 2019), and inferring heat output via concentration of chloride in runoff and streams (Ingebritsen et al., 2001). In many cases, a combination of two or more methods provides the most reliable data (Seward et al., 2018).

At least 20 geothermal fields occur in the Taupō Volcanic Zone, and the hydrothermal fluid-flow paths of the associated geothermal systems are controlled by the supply of deep magmatic heat (Rowland & Simmons, 2012). Most of the geothermal systems are found between the two active silicic magmatic centres, Ōkataina and Taupō calderas (Figure 1), and their typical 10 to 15 km spacing is notably twice the seismogenic depth, which together with rheologic arguments indicates that fluid circulation extends the full depth of the seismogenic zone (Bibby et al., 1995). The position and footprint of geothermal systems in the TVZ were delimited using images of electrical conductivity (Bibby et al., 1995). Two elongated zones of low resistivity extend from the Taupō caldera to the Ōkataina caldera parallel to the NE-SW tectonic grain. These zones bound a densely faulted region on the west side of the Central Taupō Volcanic Zone, which is devoid of present-day geothermal activity. The highest concentration of geothermal activity and convective heat transfer occurs within the Taupō-Reporoa Basin (Rowland & Simmons, 2012). Several low resistivity zones trend perpendicular to the rift axes, coinciding spatially with accommodation zones and inferred NW-striking structures in the underlying greywacke basement rock (Tienfeng & Hedenquist, 1981; Rowland & Sibson, 2004). The largest geothermal systems in the TVZ, including Waiotapu, occur associated with calderas, or at the lateral tips of major faults (Rowland & Simmons, 2012).

The Waiotapu area and its surroundings (Figure 1) are an ideal natural laboratory to examine (i) the structural control on the spatial pattern of the land surface heat flux, and (ii) the total heat and steam released from the ground at the geothermal field level. This investigation calculates the total heat and steam released from the ground surface by combining soil temperature measurements and satellite datasets.

ISSN 2703-4275

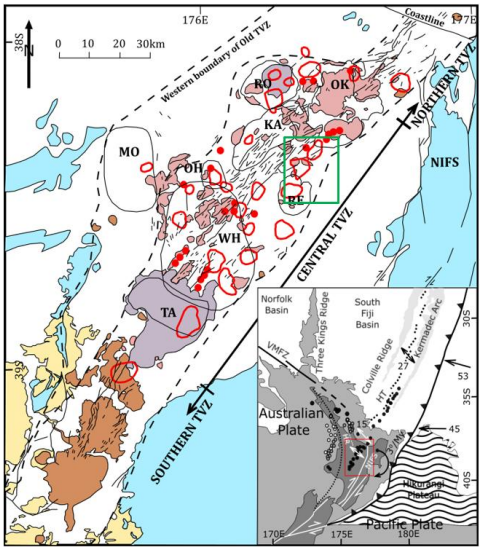

Figure 1: (a) Overview map of the Taupō Volcanic Zone (TVZ). (b) Inset map. Taken from Wilson & Rowland (2016). Solid lines: red-geothermal fields, black (closed)-inferred caldera boundary, black (open)-faults. Rock units: yellow-tertiary sedimentary rocks, brown-andesite/dacite, pink-rhyolite and genetically related dacite. Red dot: High-Al basalt. Rectangles: Green-location of Figure 2a, Red-location of Figure 1a. TA for Taupō, OK for Ōkataina, WH for Whakamaru, MO for Mangakino, KA for Kapenga, RO for Rotorua, RE for Reporoa, and OH for Ohakuri.

2. GEOLOGICAL CONTEXT

The Waiotapu study area, regionally, sits in the Taupō Volcanic Zone (TVZ), a NNE-trending rifted arc, active since ~2 Ma (Wilson et al., 1995). The TVZ represents the southernmost ~300 km-long portion (with > 40 km width) of the ~2800 km-long Tonga-Kermadec arc system (Rowland et al., 2010). The TVZ has been spatially divided into three distinct segments, including Northern, Central and Southern TVZ, with respect to the distribution of present-day volcanic systems (Wilson et al., 1995). The study area is in the Central TVZ, which is rhyolite dominant, specifically the Ngakuru subdomain of the Central domain, one of three domains making up the Central TVZ, the other two being Taupō and Ōkataina domains (Wilson & Rowland, 2016; Berryman et al., 2022). Also, the TVZ has been temporally divided into old TVZ (ca. 2 Ma up to 350 ka), young TVZ (350 ka to ~ 61 ka), and modern TVZ (61 ka to present) (Wilson et al., 1995; Wilson & Rowland, 2016). The eruption record for the Central TVZ from 61 ka (Wilson et al., 2007), with an alternative age of 45 ka (Danisík et al., 2012), is inferred to be complete, and its deposits are marker planes for present-day tectonics in the central North Island (Wilson & Rowland, 2016). Both tectonism and volcanism, discussed separately in the following two sections, have influenced the TVZ in general, thus affecting the geology of the studied area at Waiotapu.

2.1 Tectonism

High rates of extensional tectonism have resulted in the formation of two subparallel, NE-trending rift basins in the Central TVZ that are characterised by widespread subsidence of up to 25 mm yr^{-1}: the Taupō Fault Belt to the NW and the Taupō Reporoa Basin to the SE (Hamling et al., 2015). The Waiotapu Field is in the Taupō Reporoa Basin, interpreted as a simple fault-angle depression or half-graben (Downs et al., 2014) that extends along a NE strike from the Taupō volcanic centre in the SW. The Taupō Reporoa Basin is delimited in the NW by the active and geomorphically well-expressed 30 km long Paeroa Fault and its associated upstanding footwall block (Paeroa block). Along strike, beyond the southwestern limit of the Paeroa Fault, the boundary has more subdued topography, but is delimited by the active Orakei Korako, Whakaheke, and Kaiapo faults (Downs et al., 2014). The currently inactive Kaingaroa Fault zone on its eastern margin delimits the eastern extent of the Taupō Reporoa Basin.

The Paeroa Fault and its splay, Ngapouri-Rotomahana Fault, are discussed in the following sub-sections, given their significance in the studied area at regional and local scales, respectively.

(a) The Paeroa Fault

The Paeroa Fault is an important structure for understanding the tectonism associated with the studied area at Waiotapu. The 30 km-long Paeroa Fault is one of the largest and fastest slipping (c. 1.5 mm/yr vertical displacement rate) normal faults of the presently active Taupō Rift in the North Island, New Zealand (Villamor & Berryman, 2001; Berryman et al., 2008). The fault extends for 30 km along the eastern margin of the Ngakuru-Waikite depression, between the Waikato River near Orakeikorako and Waimangu on the southwestern margin of the Ōkataina caldera. Welded Paeroa ignimbrite is exposed in the up to 500 m-high fault escarpments, and this and other middle Pleistocene ignimbrite units make the Paeroa Range on the footwall of the fault. Striae on Paeroa fault planes exposed in trenches typically indicate pure dip-slip motion or variances from this of no more than 10° (Berryman et al., 2008). The fault, striking 040-050°, is mainly downthrown to the northwest, and its complexity varies significantly along the strike. It can be considered in three distinct sections: north, central, and south. Between the central and north sections, the Ngapouri Fault splays towards the northeast (Berryman et al., 2008; Berryman et al., 2022). Along the c. 7 km long southern section, the fault consists of several distributed fault strands downthrown to the northwest. The height of the Paeroa Range front-scarp increases along this sector from zero at the Waikato River to c. 200 m above the hanging wall in the vicinity of Te Kopia. In the c. 8 km long central section, the range increases in elevation and reaches a maximum of ~500 m above the hanging wall. In this section, the fault has two primary strands, all downthrown to the northwest. Some of the displacement on the Paeroa Fault may be transferred on to the Ngapouri Fault, which may explain the reduction in range-front height from this point northward.

(b) Ngapouri-Rotomahana Fault

The 15 km-long Ngapouri-Rotomahana Fault is a significant structure that potentially exerts control on surface heat flux at Waiotapu. It extends to the southern boundary of the Ōkataina Volcanic Centre, as demarcated by the Haroharo caldera boundary, near the eastern margin of the Taupō Rift. From this location, the Ngapouri-Rotomahana Fault extends to the southwest through the northern margin of the Waiotapu geothermal field to join the Paeroa Fault. Neither the Paeroa Fault nor the Ngapouri-Rotomahana Fault is exactly on-trend

with the Tarawera vent zone, though together, these faults envelop the south-westward extent of this volcanic feature (Berryman et al., 2022). The Ngapouri-Rotomahana Fault traces are observed as 1–5 m high scarps across low basins and valleys where Holocene airfall tephra, the 232 CE Taupō ignimbrite and pyroclastic sediments from neighbouring explosion craters have infilled older topography by 3–5 m. Large and broad scarps are observed in older topography. Berryman et al. (2022) highlighted that the kinematics along the Ngapouri-Rotomahana Fault cannot be resolved accurately due to the paucity of striae observed on fault planes and geomorphic piercing points with relatively smooth topography resulting from tephra and alluvial infill. While the traces of the Ngapouri-Rotomahana Fault exhibit essentially normal displacement, a small strike-slip component likely occurs, such that thickness variations across a fault plane may partly result from minor out-of-plane displacement. At other places in the region, the sparse striae in fault trench exposures and geomorphic piercing points support, within small margins, up to 10^0 of obliquity, in predominantly normal faulting (Berryman et al., 2008).

2.2 Volcanism

The Central TVZ, where the study area sits, hosts an exceptionally vigorous active hydrothermal province with a present-day average heat flow of 700 mW/m^2 (Bibby et al., 1995; Seebeck & Nicol, 2009) and total flux of 4.2 GW, together with a volcanic output of large caldera-forming eruptions alone exceeding 6000 km^3 of rhyolitic magma during the Quaternary (Rowland et al., 2010). About four times as much magma is trapped at depth below the Central TVZ than erupted. The volcanism of the Central TVZ can be described using three time periods, specifically the old, young, and modern TVZ. The rocks of the old TVZ, overlying the greywacke basement, predates the regional marker horizon of the Whakamaru Group ignimbrites, and the pyroclastic units from this period are collectively grouped as the Tahorakuri Formation, a part of the Reporoa Group (Gravley et al., 2006). The volcanic activity defining young TVZ includes and postdates a cluster of seven major caldera-forming and many more minor eruptions between ~350 and ~280 ka, totalling >3000 km^3 of magma, and forming calderas over a collective 90 × 40 km^2 area (Downs et al., 2014). Currently, at least eight calderas can be identified, including Taupō (active), Ōkataina (active), Whakamaru, Mangakino, Kapenga, Rotorua, Reporoa, and Ohakuri calderas (Wilson & Rowland, 2016; Downs et al., 2014; Rowland et al., 2010). The products of other volcanic activity, from 340 to ~61 ka, are visually prominent in the present day in the form of rhyolite domes that occur throughout the Central TVZ (Wilson & Rowland, 2016). Volcanism of modern TVZ is taken to represent the current condition of the Central TVZ regarding the styles and scales of volcanism, as well as compositions of eruptives (Wilson & Rowland, 2016). The active volcanoes for the modern TVZ represent the primary source of volcanic hazards to people and infrastructure, and by far, most eruptions came from Taupō and Ōkataina volcanoes.

The Ōkataina Volcanic Centre is a likely strong influence on the Waiotapu field. Volcanism has been active for ~625 kyr and magmatism for up to ~750 kyr (Cole et al., 2014). The centre comprises a complex of coalescing collapse structures resulting from at least two large caldera-forming events, the 150 km^3 Matahina (ca. 322 ka) and the ~100 km^3 Rotoiti (for which dates of 61 and 45 ka are debated). Pyroclastic eruptions comprise ~50% of the total erupted from the centre (Wilson et al., 2007; Cole et al., 2014). In addition, Cole et al. (2014) postulated two other possible collapse events: Utu, ~557 ka; and Kawerau, ~33 ka events in the centre. The style of activity at Ōkataina Volcanic Centre changed at ~25 ka and has been typified by eruptions from multiple vents along two sub-parallel NE-trending vent zones that transect the caldera complex (Cole et al., 2014). The Haroharo Dome Complex, in the north of Ōkataina Volcanic Centre, formed in the last 25 ka during five key eruptive episodes. The similar Tarawera Dome Complex occupies the southern part of Ōkataina Volcanic Centre. It has five recorded eruptive episodes during the last 22 ka, culminating with the 1886 AD basaltic eruption (Shane et al., 2008).

Recent eruptions at the Ōkataina Volcanic Centre involved the 1886 AD basaltic eruption preceded by the 1314 ± 12 CE Kaharoa rhyolitic event. In 1886, the ~ 17 km-long and 057^o trending basaltic dyke reached the ground surface to form en-echelon craters at Mt. Tarawera and extended southwest under Lake Rotomahana to Waimangu (Seebeck & Nicol, 2009). At Waimangu, phreatomagmatic and hydrothermal explosions were triggered along a linear zone. However, hot springs at the Waiotapu area, only a few kilometres off-trend and to the south of Waimangu, did not seem to change, indicating there was no longer pressure in the geothermal system despite ongoing fumarolic activity and many hot springs. The 1314 ± 12 CE (Lowe et al., 2013) eruption event was primed and triggered by repeated basalt dyke intrusions into a pre-existing rhyolite magma body (Nairn et al., 2005). Explosion breccias erupted from a series of craters in the Waiotapu area (Nairn et al., 2005; Montanaro et al., 2020). The main explosion craters are Lakes Okaro, Opal, Ngahewa, Opouri, and Tutaeinanga (all now cold), which are all near the Ngapouri-Rotomahana Fault, and Lake Ngakoro and Champagne Pool (warm to hot temperature) in the Waiotapu geothermal field. Nairn et al. (2005) highlighted a close temporal association between the hydrothermal eruptions at Waiotapu and the magmatic Kaharoa eruption at Tarawera. Cross (1963) mapped the breccia deposits around the explosion craters and showed that while these vents were active for a short period, they were sequential rather than simultaneous – for instance, the Okaro breccia overlies the Opal breccia and the Tutaeinanga breccia overlies the Opouri breccia.

3. METHODS

3.1 Fault Analyses

The structural fabric of both Waiotapu and the surrounding region of the rift was investigated at regional and local scales and correlated with the 2D spatial distribution of land surface temperatures to evaluate controls on hot fluid flow at the Waiotapu area. The open topography DEM downloader plugin and Hillshade algorithm in QGIS were used to analyse the structural fabrics for the studied area from the 30 m-resolution Shuttle Radar Topography Mission (SRTM) DEM dataset.

Faults were identified after processing the DEM using QGIS software for the Waiotapu area and the surrounding regions. Similar to other fault studies in the rift setting (e.g., Williams et al., 2022), our fault mapping approach considers an active fault as any fault that has an indication for displacement during the Taupō Volcanic Zone rifting or is buried beneath the rift valley and is favourably oriented to the regional stresses (Williams et al., 2022). Geological maps, previous literature, and satellite imagery are also used to support the analysis of the relatively high-resolution topography

(Wedmore et al., 2024). Each fault is mapped as following the fault escarpment, with fault tips indicated as the points at which a fault no longer has a detectable topographic expression (Williams et al., 2022). The fault dip direction is determined using the 'facing direction', considered as facing the downthrown side of the fault.

3.2 Satellite Data Analysis

The Landsat 9 dataset is used to estimate the total heat flux for the studied area**.** The heat flux is calculated for the study area using the computed Land Surface Temperatures from Landsat 9 raw data. The Landsat 9 data are initially preprocessed to correct for atmospheric and radiometric effects and then processed using emissivity and land surface temperature calculations (Darge et al., 2019). Radiometric calibration and atmospheric correction are made for Landsat 9 OLI red (band 4), OLI near-infrared (band 5) and TIRS thermal infrared (bands 10 and 11). Radiometric calibration is carried out to convert the digital number recorded by the remote sensors into the at-atmosphere radiance images. The radiance multiplicative scaling factor and radiance additive scaling factor are retrieved from the Metadata of Landsat 9 to compute the spectral radiance.

The 6S model (Vermote et al., 1997) is also applied in this study for the atmospheric correction on the two multispectral bands by defining the geometry of the satellite observation, viewing angle and other necessary datasets. The minimum dataset to run the 6S model is the meteorological visibility, type of sensor, sun zenith and azimuth angles, date and time of image acquisition, atmospheric model, spectral condition, target and sensor altitude, ground reflectance, and latitude and longitude of scene centre (Darge et al., 2019). Most of these parameters were gathered from the metadata file of an image. Using the input data and embedded features, the model produces atmospheric model descriptions and variables to assess estimated variables, such as water vapour content. The true reflectance value is determined from the model output (Darge et al., 2019).

The Landsat 9 data are processed using emissivity and land surface temperature calculations. The Land Surface Emissivity (LSE) is determined by applying the NDVI thresholds method, which is a pixel-level emissivity calculation method (Chatterjee et al., 2017; Darge et al., 2019). The emissivity is calculated according to Eq. (1) as the area is covered by soil and vegetation. While E_v and E_s in Eq. (1) are the soil and vegetation emissivity, respectively, P_v is the proportion of vegetation, also referred to as fractional vegetation cover, and represents the percentage of the vertical projection of the vegetation canopy (including leaves, stems, and branches) in per unit area (Darge et al., 2019).

$$E_\lambda = E_v P_v + E_s (1 - P_v) + C_\lambda \qquad (1)$$

After calculating the LSE for both bands of TIR, the mean (EM) and difference (ΔE) Land Surface Emissivity (LSE) (parameters for estimating the Land Surface Temperature (LST)) are calculated from Eq. (2) and (3) (Sobrino et al., 2008), with E_{10} and E_{11} for the LSE of band 10 and 11. The Split Window (SW) algorithm is used to retrieve the LST. The SW algorithm is based on the mathematical structure suggested by Sobrino et al. (1996) and applied to various Earth observation sensors (Sobrino et al., 2008; Romaguera et al., 2018). The algorithm uses the brightness temperature of two TIR bands, mean and difference in LSE as indicated by Eq. (4). Whereas the T_s in Eq. (4) is the LST in Kelvin, the T_i and T_j are the at-sensor brightness temperatures in the SW bands 10 and 11. The W is the total atmospheric water vapour content, which was retrieved from the 6S model. The C_0 - C_6 are the SW coefficient values (Skokovic et al., 2014).

$$EM = (E_{10} + E_{11})/2 \qquad (2)$$

$$\Delta E = E_{10} - E_{11} \qquad (3)$$

$$T_s = T_i + C_1(T_i - T_j) + C_2(T_i - T_j)^2 + C_0 + (C_3 + C_4 W)(1-EM) + (C_5 + C_6 W)\,\Delta E \qquad (4)$$

3.3 Shallow (15 cm) Temperature Estimation from Landsat 9 Surface Temperatures

Land surface temperatures calculated from the Landsat 9 dataset, with an achievable spatial resolution of 30 m x 30 m through resampling, are calibrated using 422 shallow (15cm) temperatures measured on the ground in the studied area. Using a geothermal gradient ranging from 25ºC/km to 300ºC/km for sensitivity analysis, temperatures measured at 15 cm slightly change relative to the land surface temperature that would be measured at each respective point, assuming that conduction is the dominant heat transfer mechanism for the thin 15 cm surface layer that is mostly above the water table. The QGIS point sampling tool is used to determine temperatures at 422 points (exact locations where shallow temperature measurements were carried out) from the calculated Landsat 9 surface temperature map. Before determining the relationship between two variables, temperatures from ground measurements and Landsat 9-point sampling are normalised using three approaches (minimum-maximum scaling**,** log transformation, and z-score standardisation). The determined relationship from the bivariate analysis is applied to calibrate the land surface temperatures from Landsat 9 thermal imagery to the likely surface temperatures on the ground, thus approximating shallow (15cm) temperatures.

3.4 Total Heat and Steam Calculations

The total heat and steam released for the studied area are determined from the estimated shallow (15 cm) temperatures. The heat flux spatial distribution is calculated from the spatial pattern of the estimated shallow temperatures by using Eq. (5), where q is the heat flux in W m^{-2} at the soil surface, C is the empirical constant in W $m^{-2}/ºC^4$ and t_{15} is the soil temperature at 15 cm depth in ºC (Dawson, 1964; Fridriksson et al., 2006; Taussi et al., 2021). The raster surface volume calculation in QGIS is used to calculate the total heat flux from the 2D spatial spread of heat fluxes. The steam flux is inferred using Eq. (6), assuming the measured heat flux results from the sum of (i) condensation of steam in the shallow subsurface (conductive heat flux) and (ii) convective steam flux (Fridriksson et al., 2006; Harvey et al., 2017). While F_{stmq} in Eq. (6) is the steam flux (kg s^{-1}), q_m is the arithmetic mean of thermal ground heat flux (kJ m^{-2} s^{-1}) estimated from Eq. (5), A is the studied area (m^2), HV,98 ºC (672.4 kJ/Kg; Zarrouk & Watson, 2010) is the enthalpy of steam at 98ºC (i.e. the approximate boiling point of water at the Waiotapu altitude), and HL,12 ºC (50.4 kJ/Kg; Zarrouk & Watson, 2010) is the enthalpy of liquid water at the mean ambient temperature in the studied area.

$$q = C \times t_{15}^4 \qquad (5)$$

$$F_{stmq} = q_m \times A \times (H_{V,98\,^oC} - H_{L,12\,^oC})^{-1} \qquad (6)$$

ISSN 2703-4275

4. RESULTS

4.1 Structural Fabrics

Geological structures were mapped at the Waiotapu area and its surroundings at regional and local levels using the combined DEM and Hillshade raster layers (Figure 2). Tectonic structures, including fault belts (e.g., Taupō Fault Belt) and basins (e.g., Taupō Reporoa Basin), were identified. The structural trend of the faults is predominantly NE-SW, typical for the Taupō Volcanic Zone, and some fault structures trend NW-SE and NNW-SSE. Volcanic structures, particularly volcanic cones and lineation, are also mapped from their topographic expression. The major fault structures, the Paeroa Fault and Ngapouri-Rotomahana Fault, strike NE-SW with a NW dip direction and have significantly influenced the topography of the studied area.

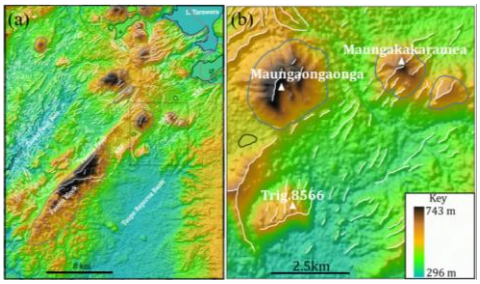

Figure 2. A map showing geological (tectonic and volcanic) structures at Waiotapu and its surroundings. (a) Regional scale. (b) Local scale. NRF-Ngapouri Rotomahana Fault. Solid lines: white – faults, blue-topographic highs, purple-caldera rim, and black-lakes. The black rectangle in (a) is for the location of (b).

4.2 2D Spatial Pattern of Land Surface Temperatures

The 2D spatial distribution of land surface temperature is influenced by geological (tectonic and volcanic) structures in the Waiotapu area and its surroundings (Figure 3). The distribution of hot temperature anomalies is affected by the trend of normal faults, including the NE-SW trending Paeroa Fault and Ngapouri-Rotomahana Fault. Hot temperature anomalies are commonly found on the hanging wall side of normal fault structures compared to the footwall, and relatively low temperatures characterise the fault scarp. Footwall areas are commonly in zones of poor drainage/water bodies or surface water-saturated soils, and this could dampen the heat flux. Tectonic uplifting also controls the spatial pattern of land surface temperatures in the study area, as topographic highs, including the Paeroa fault block, are associated with low-temperature anomalies.

Volcanic structures, including cones, have also affected the 2D spatial spread of land surface temperatures (Figure 3). Topographic highs associated with volcanic cones or dome structures are sometimes associated with low-temperature anomalies, including Maungaongaonga and Maungakakaramea at Waiotapu. Though active volcanic cones may be associated with high-temperature anomalies, the effect of elevation on the land surface temperature can be a dominating factor, especially for dormant or passive volcanoes. Some topographic highs associated with volcanic structures, including the Trig. 8566 volcanic dome, are alternatively associated with high-temperature anomalies.

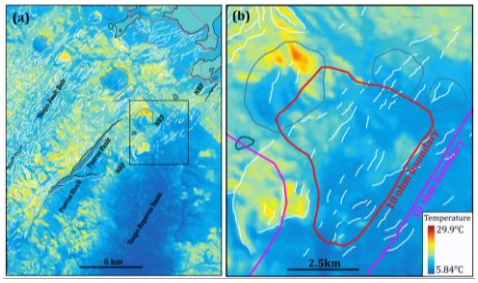

Figure 3. A map showing the calculated surface temperature patterns at (a) the regional scale and (b) the local scale. For the key, see Figure 2.

4.3 Relationship between Landsat 9 temperatures and ground temperature measurements

The relationship between the calculated Landsat 9 land surface temperatures (Tspl) and ground temperature measurements (Tgrn) is determined using three data normalisation approaches, considering linear and non-linear relationships between the two variables. The data analysed are noisy, but it appears that the two variables have a weak positive trend. Three linear relationships are calculated for three different normalisation techniques, including minimum-maximum (min-max) scaling (Eq. (7)), log transformation (Eq. (8)), and z-score standardisation (Eq. (9)). The fitted non-linear relationship, which looks like an exponential growth curve, is also approximated to linear relationships over different defined intervals (e.g., L1, L2, and L3 in Figure 4 (a)) in each case.

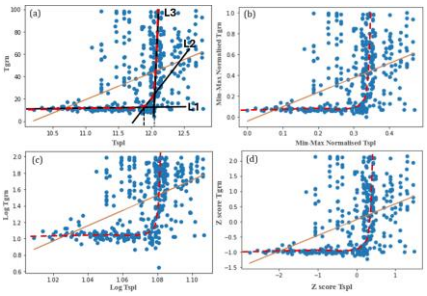

Figure 4. The plot of sampled land surface temperatures from Landsat 9 versus ground temperature measurements at the exact point locations. (a) Before normalisation. (b) Using minimum-maximum scaling. (c) Log transformation. (d) Z-score standardisation. Solid light brown line for linear fit, dashed red curve for non-linear fit, and solid black lines (L1-L3) for approximating non-linear fit by linear fit over defined intervals.

$$Y = 1.389X - 0.043 \quad (7)$$

$$Y = 9.313X - 8.530 \quad (8)$$

$$Y = 0.520X + 0.059 \quad (9)$$

4.4 Estimated Heat and Steam Release at Waiotapu Geothermal Field

Total heat flux and steam release from the ground surface are calculated for the Waiotapu geothermal field (Table 1). The 10-ohm resistivity boundary is used in the calculations to define the areal extent of the geothermal field. Also, the linear relationships from all three normalisation techniques are

applied to estimate the total heat flux and steam release from the ground surface.

Table 1. Calculated heat flux and steam release for the Waiotapu geothermal field.

	Heat flux (MW_{th})	Steam releases (kt/s)
Min-max scaling	527.4	11746.9
Log transformation	273.9	3592.1
Z-score standardisation	567.6	12831.5

5. DISCUSSION

5.1 Structural Control on the Spatial Spread of the Ground Surface Heat Fluxes

Geological structures, from tectonic and volcanic origins, can facilitate the migration of hot fluids to the surface or control the surface topography. The migrated hot geofluids through active structures, including normal faults and volcanic vents, affect the ground surface temperatures, and they can be mapped as hot anomalous areas. Topographic elements (elevation, aspect, and slope) also influence the ground surface temperatures (He et al., 2019). The elevation and land surface temperature can have an inverse relationship; hot anomalies mapped from active volcanic cones/domes or uplifted fault blocks would underestimate the actual heat flux from the migrated hot fluids due to the elevation effect. The high surface water accumulation in low points, such as fault footwalls, could also hide some heat. Future work needs to examine how to eliminate the topographic effect to quantify the actual heat flux from the migrating hot fluids.

Other factors influence the ground surface temperatures, including surface solar radiation and temporal variabilities. Though the study assumed the minimal influence of sun radiation on the calculated ground surface temperatures, examining how sensitive the sun radiation effect is on the calculated surface temperatures in future work will be essential. This investigation has also considered minimal temporal changes in the heat fluxes relative to the time discrepancy for ground and Landsat 9 data collection. The Landsat 9 data used in this study were collected on the same day the ground measurements were taken to reduce the influence of temporal variabilities in the heat fluxes.

5. 2 Calibration of Surface Temperatures from Landsat 9 using Actual Temperature Measurements

Surface temperatures calculated from the Landsat 9 dataset are smaller than ground temperature measurements at the exact locations, as each calculated temperature is per 900 m^2 pixel size and, thus, an average temperature from various points of that area is obtained. A calibration approach is suggested by fitting the linear and non-linear relationship models between calculated temperatures from the Landsat 9 and ground temperature measurements at the exact point locations. Temperature data for the two variables are normalised to ensure a fair comparison and prevent a certain variable from dominating the analysis. Though the fitted non-linear relationship model is more convincing than the single straight-line model, it is defined over a narrow range of sampled surface temperatures from the Landsat 9 thermal map. The fitted single straight-line model is considered to have a rough estimate of the heat flux for the study area, as the model is defined at all temperatures sampled from the Landsat 9 thermal map (T_{spl}). However, there is no clear relationship between the sampled Landsat 9 temperatures (T_{spl}) and ground temperature measurements (T_{grn}), and this could be due to the spatial heterogeneity mismatch, sampling regime, and time matching.

The ground temperature measurements used for the calibration were measured at 15 cm (shallow depth), and by conducting a sensitivity analysis, these temperatures are nearly equal to temperatures measured on the ground surface. Using geothermal gradients of 25°C/km and 300°C/km, the normal and anomalous temperature gradients, respectively, the temperature increase at 15 cm depth ranges between $3.75*10^{-3}$ °C and $4.50*10^{-2}$ °C, assuming conduction as the dominant heat transfer mechanism in the thin (15 cm) layer that is likely to be above the water table. The slight temperature increase justifies the approximation of shallow (15cm) temperature measurements to temperatures that would be measured on the surface at the same location points.

5.3 Total Heat and Steam Released from the Waiotapu Geothermal Field

Total heat and steam release estimates by applying minimum-maximum scaling and z-score standardisation are almost equal at ±3.7% and ±4.4% on average, respectively. Total heat and steam release, calculated using the equation associated with log transformation, are underestimated as the exponential function (inverse of logarithmic function) produces many pixel-level temperature values that are very high or very low with a low likelihood of being measured on the ground and thus filtered out. The Waiotapu geothermal field extent could be delineated by a range of mapped resistivity boundaries (Rowland & Simmons, 2012; Rodriguez-Gomez et al., 2021; Seward et al., 2025). The 10-ohm resistivity boundary is used in this investigation as a conservative estimate of the areal extent of the field. Increasing the area of the geothermal field (e.g., use of a 15-ohm or 30-ohm boundary) would obviously markedly increase estimates of heat and steam release.

The total heat flux of 547.5 ± 20.1 MW, calculated by using minimum-maximum scaling and z-score standardisation, is slightly higher than the historically estimated heat loss, ranging between 410 and 520 MW, using a variety of methods (Seward et al., 2025). Thus, the approach described in this study is promising for heat flux and steam release calculation for other geothermal fields of the Taupō Volcanic Zone.

5. CONCLUSION

Tectonic and volcanic structures influence the heat flux and steam release at the Waiotapu geothermal field in the Taupō Volcanic Zone. Faults trending NE-SW, NW-SE, and NNW-SSE provide permeable pathways that allow the migration of hot fluids, thus making the estimation of overall heat flux and steam release complex. Tectonic uplifting generally negatively affects land surface temperatures, estimated heat flux and steam released, while volcanic structures may facilitate higher heat flows. Also, topographic highs associated with volcanic structures negatively influence the calculated land surface temperatures, due to the elevation effect on temperature. These features control the 2D spatial pattern of land surface temperatures, heat flux and steam release of the region.

Total heat flux and steam release are estimated for the Waiotapu geothermal field using calculated land surface temperatures and shallow temperature ground measurements. Calculated land surface temperatures from the Landsat 9 dataset are calibrated using ground measurements with various data normalisation approaches, specifically minimum-maximum scaling, log transformation, and z-score standardisation. Total heat flux and steam release calculated for the Waiotapu geothermal field in this study are 547.5 ±20.1 MW and 12.3 ± 0.5 Mt/s, respectively. The heat flux is slightly higher than historically estimated values (410 to 520 MW), even using a conservative value for the field boundary.

ACKNOWLEDGEMENTS

The authors gratefully acknowledge the anonymous reviewers for their insightful comments on this work. Thank you to the University of Auckland for the continuing support in this effort. We also acknowledge funding support from the MBIE Research Programme UOAX2213: Adapting to climate change through stronger geothermal enterprises.

REFERENCES

Berryman, K., Villamor, P., Nairn, I., Begg, J., Alloway, B. V., Rowland, J., ... & Capote, R. (2022). Volcano-tectonic interactions at the southern margin of the Okataina Volcanic Centre, Taupō Volcanic Zone, New Zealand. *Journal of Volcanology and Geothermal Research*, *427*, 107552.

Berryman, K., Villamor, P., Nairn, I., Van Dissen, R., Begg, J., & Lee, J. (2008). Late Pleistocene surface rupture history of the Paeroa fault, Taupo rift, New Zealand. *New Zealand Journal of Geology and Geophysics*, *51*(2), 135-158.

Bibby, H. M., Caldwell, T. G., Davey, F. J., & Webb, T. H. (1995). Geophysical evidence on the structure of the Taupo Volcanic Zone and its hydrothermal circulation. *Journal of volcanology and geothermal research*, *68*(1-3), 29-58.

Bromley, C.J., Ashraf, S., Seward, AM., Reeves, R., 2015. Monitoring and quantifying heat loss from significant geothermal areas via remote sensing. In: *Proceedings of 37th New Zealand Geothermal Workshop*, Taupo, New Zealand.

Chatterjee, R. S., Singh, N., Thapa, S., Sharma, D., & Kumar, D. (2017). Retrieval of land surface temperature (LST) from Landsat TM6 and TIRS data by single channel radiative transfer algorithm using satellite and ground-based inputs. *International journal of applied earth observation and geoinformation*, *58*, 264-277.

Cole, J. W., Deering, C. D., Burt, R. M., Sewell, S., Shane, P. A. R., & Matthews, N. E. (2014). Okataina Volcanic Centre, Taupo Volcanic Zone, New Zealand: a review of volcanism and synchronous pluton development in an active, dominantly silicic caldera system. *Earth-Science Reviews*, *128*, 1-17.

Cross, D. (1963). Soils and geology of some hydrothermal eruptions in the Waiotapu district. *New Zealand journal of geology and geophysics*, *6*(1), 70-87.

Danisík, M., Shane, P., Schmitt, A.K., Hogg, A., Santos, G.M., Storm, S., Evans, N.J., Fifield, L.K., Lindsay, J.M., 2012. Re-anchoring the late Pleistocene tephrochronology of New Zealand based on concordant radiocarbon ages andcombined238U/230Th disequilibrium and (U–Th)/He zircon ages. Earth Planet.Sci. Lett. 349, 240–250.

Darge, Y. M., Hailu, B. T., Muluneh, A. A., & Kidane, T. (2019). Detection of geothermal anomalies using Landsat 8 TIRS data in Tulu Moye geothermal prospect, Main Ethiopian Rift. *International Journal of Applied Earth Observation and Geoinformation*, *74*, 16-26.

Dawson, G. B. (1964). The nature and assessment of heat flow from hydrothermal areas. *New Zealand Journal of Geology and Geophysics*, *7*(1), 155-171.

Downs, D.T., Rowland, J.V., Wilson, C.J.N., Rosenberg, M.D., Leonard, G.S., Calvert, A.T., 2014. Evolution of the intra-arc Taupo-Reporoa Basin within the Taupo Volcanic Zone of New Zealand. Geosphere 10, 185–206.

Fridriksson, T., Kristjánsson, B. R., Ármannsson, H., Margrétardóttir, E., Ólafsdóttir, S., & Chiodini, G. (2006). CO2 emissions and heat flow through soil, fumaroles, and steam heated mud pools at the Reykjanes geothermal area, SW Iceland. *Applied geochemistry*, *21*(9), 1551-1569.

Gravley, D. M., Wilson, C. J. N., Rosenberg, M. D., & Leonard, G. S. (2006). The nature and age of Ohakuri Formation and Ohakuri Group rocks in surface exposures and geothermal drillhole sequences in the central Taupo Volcanic Zone, New Zealand. *New Zealand Journal of Geology and Geophysics*, *49*(3), 305-308.

Hamling, I. J., Hreinsdóttir, S., & Fournier, N. (2015). The ups and downs of the TVZ: Geodetic observations of deformation around the Taupo Volcanic Zone, New Zealand. *Journal of Geophysical Research: Solid Earth*, *120*(6), 4667-4679.

Harvey, M. C., Rowland, J. V., Chiodini, G., Rissmann, C. F., Bloomberg, S., Fridriksson, T., & Oladottir, A. A. (2017). CO2 flux geothermometer for geothermal exploration. *Geochimica et Cosmochimica Acta*, *213*, 1-16.

He, J., Zhao, W., Li, A., Wen, F., & Yu, D. (2019). The impact of the terrain effect on land surface temperature variation based on Landsat-8 observations in mountainous areas. *International Journal of Remote Sensing, 40*(5-6), 1808-1827.

Hochstein, M. P., & Bromley, C. J. (2005). Measurement of heat flux from steaming ground. *Geothermics*, *34*(2), 131-158.

Ingebritsen, S.E., Galloway, D.L., Colvard, E.M., Sorey, M.L., Mariner, R.H., 2001. Time variation of hydrothermal discharge at selected sites in the western United States: implications for monitoring. Journal of Volcanology and Geothermal Research 111 (1–4), 1–23.

Lowe, D. J., Blaauw, M., Hogg, A. G., & Newnham, R. M. (2013). Ages of 24 widespread tephras erupted since 30,000 years ago in New Zealand, with re-evaluation of the timing and palaeoclimatic implications of the Lateglacial cool episode recorded at Kaipo bog. *Quaternary Science Reviews*, *74*, 170-194.

Montanaro, C., Ray, L., Cronin, S. J., Calibugan, A., Rott, S., Bardsley, C., & Scheu, B. (2023). Linking top and subsoil types, alteration and degassing processes at

Rotokawa geothermal field, New Zealand. *Frontiers in Earth Science*, *10*, 1067012.

Nairn, I. A., Hedenquist, J. W., Villamor, P., Berryman, K. R., & Shane, P. A. (2005). The~ AD1315 Tarawera and Waiotapu eruptions, New Zealand: contemporaneous rhyolite and hydrothermal eruptions driven by an arrested basalt dike system? *Bulletin of Volcanology*, *67*, 186-193.

Romaguera, M., Vaughan, R. G., Ettema, J., Izquierdo-Verdiguier, E., Hecker, C. A., & Van der Meer, F. D. (2018). Detecting geothermal anomalies and evaluating LST geothermal component by combining thermal remote sensing time series and land surface model data. *Remote Sensing of Environment*, *204*, 534-552.

Rowland, J. V., & Sibson, R. H. (2004). Structural controls on hydrothermal flow in a segmented rift system, Taupo Volcanic Zone, New Zealand. *Geofluids*, *4*(4), 259-283.

Rowland, J. V., & Simmons, S. F. (2012). Hydrologic, magmatic, and tectonic controls on hydrothermal flow, Taupo Volcanic Zone, New Zealand: implications for the formation of epithermal vein deposits. *Economic Geology*, *107*(3), 427-457.

Rowland, J. V., Wilson, C. J., & Gravley, D. M. (2010). Spatial and temporal variations in magma-assisted rifting, Taupo Volcanic Zone, New Zealand. *Journal of Volcanology and Geothermal Research*, *190*(1-2), 89-108.

Seward, A. M., Reeves, R. R., Mroczek, E., Macdonald, N., & Brakenrig, T. (2025). Surface heat loss assessment at the Waiotapu Geothermal Field, Taupo Volcanic Zone, New Zealand. *Geothermics*, *126*, 103205.

Seward, A., Ashraf, S., Reeves, R., & Bromley, C. (2018). Improved environmental monitoring of surface geothermal features through comparisons of thermal infrared, satellite remote sensing and terrestrial calorimetry. *Geothermics*, *73*, 60-73.

Shane, P., Nairn, I.A., Smith, V.C., Darragh, M., Beggs, K.F., Cole, J.W., 2008. Silicic recharge of multiple rhyolite magmas by basaltic intrusion during the 22.6 ka Okareka eruption episode, New Zealand. Lithos 103, 527–549.

Skokovic, D., Sobrino, J. A., Jiménez-Muñoz, J. C., Sòria, G., Julien, Y., Mattar, C., & Jordi, C. (2014). Calibration and Validation of land surface temperature for Landsat 8-TIRS sensor. Land Product Validation and Evolution.

Sobrino, J. A., Jiménez-Muñoz, J. C., Sòria, G., Romaguera, M., Guanter, L., Moreno, J., ... & Martínez, P. (2008). Land surface emissivity retrieval from different VNIR and TIR sensors. *IEEE transactions on geoscience and remote sensing*, *46*(2), 316-327.

Taussi, M., Nisi, B., Vaselli, O., Maza, S., Morata, D., & Renzulli, A. (2021). Soil CO2 flux and temperature from a new geothermal area in the Cordón de Inacaliri Volcanic Complex (northern Chile). Geothermics, 89, 101961.

Tienfeng, W., & Hedenquist, J. W. (1981). A reassessment of the structural control of the Broadlands geothermal field, New Zealand. In *New Zealand geothermal workshop* (pp. 195-202).

Vermote, E.F., Tanre, D., Deuze, H.M., & Morcrette, J. (1997). Second simulation of the satellite signal in the solar spectrum, 6s: an overview. IEEE Trans. Geosci. Remote Sens. 35, 675–686.

Villamor, P., & Berryman, K. (2001). A late Quaternary extension rate in the Taupo Volcanic Zone, New Zealand, derived from fault slip data. *New Zealand Journal of Geology and Geophysics*, *44*(2), 243-269.

Wang, Y., Pang, Z., 2023. Heat flux in volcanic and geothermal areas: Methods, principles, applications and future directions. Gondwana Research 122, 260–278.

Wang, Y., Pang, Z., Hao, Y., Fan, Y., Tian, J., Li, J., 2019. A revised method for heat flux measurement with applications to the fracture-controlled Kangding geothermal system in the Eastern Himalayan Syntaxis. Geothermics 77, 188–203.

Wedmore, L. N., Evans, D., Williams, J. N., Biggs, J., Fagereng, Å., Mawejje, P., & Hobley, D. E. (2024). The early onset of magmatic rift faulting in the Edward-George Rift, Uganda. *Earth and Planetary Science Letters*, *638*, 118762.

Williams, J. N., Wedmore, L. N., Scholz, C. A., Kolawole, F., Wright, L. J., Shillington, D. J. & Werner, M. J. (2022). The Malawi active fault database: An onshore-offshore database for regional assessment of seismic hazard and tectonic evolution. *Geochemistry, Geophysics, Geosystems*, *23*(5), e2022GC010425.

Wilson, C. J. N., Houghton, B. F., McWilliams, M. O., Lanphere, M. A., Weaver, S. D., & Briggs, R. M. (1995). Volcanic and structural evolution of Taupo Volcanic Zone, New Zealand: a review. *Journal of volcanology and geothermal research*, *68*(1-3), 1-28.

Wilson, C. J., & Rowland, J. V. (2016). The volcanic, magmatic and tectonic setting of the Taupo Volcanic Zone, New Zealand, reviewed from a geothermal perspective. *Geothermics*, *59*, 168-187.

Wilson, C.J.N., Rhoades, D.A., Lanphere, M.A., Calvert, A.T., Houghton, B.F., Weaver, S.D., Cole, J.W., 2007. A multiple-approach radiometric age estimate for the Rotoiti and Earthquake Flat eruptions, New Zealand, with implications for the MIS 4/3 boundary. Quat. Sci. Rev. 26, 1861–1870.

Yang, T. H. J., Chambefort, I., Rowe, M., Mazot, A., Seward, A., Werner, C., ... & Sander, F. (2024). Variability in surface CO2 flux: Implication for monitoring surface emission from geothermal fields. *Geothermics*, *120*, 102981.

Zarrouk, S., & Watson, A. (2010). Thermodynamic and transport properties of saturated steam and water.